Transverse Failure of Unidirectional Composites: Sensitivity to Interfacial Properties

S. Zacek[a], D. Brandyberry[a], A. Klepacki[c], C. Montgomery[b], M. Shakiba[a], M. Rossol[b], A. Najafi[c], X. Zhang[a], N. Sottos[b,d], P. Geubelle[a,d,*], C. Przybyla[e], G. Jefferson[e]

[a] *Department of Aerospace Engineering, University of Illinois, Urbana, IL, USA*
[b] *Department of Materials Science and Engineering, University of Illinois, Urbana, IL, USA*
[c] *Department of Mechanical Science and Engineering, University of Illinois, Urbana, IL, USA*
[d] *Beckman Institute of Advanced Science and Technology, University of Illinois, Urbana, IL, USA*
[e] *Air Force Research Laboratory, Wright-Patterson AFB, OH, USA*

Abstract

A computational framework is developed to model the transverse failure of fiber-reinforced polymer-matrix composites, with an emphasis on capturing fiber debonding with a cohesive failure model along the fiber/matrix interfaces. We introduce a nonlinear material sensitivity formulation to quantify how variations in the interfacial cohesive zone properties affect the transverse failure response. The analytic sensitivity formulation is implemented in an Interface-enriched Generalized Finite Element Method (IGFEM) framework that allows for the simulation of transverse failure in a composite layer consisting of hundreds of closely packed fibers discretized with finite element meshes that do not need to conform to the composite microstructure.

Keywords: Polymer-matrix composites (A), Transverse cracking (C), Computational mechanics (C), Analytical sensitivity, Carbon fiber (A)

---

1. Introduction

In fiber-reinforced polymer-matrix composite laminates, transverse plies are needed to provide stiffness and strength under multi-axial loading. However, unidirectional plies typically have a relatively low transverse strength [1]. Transverse cracking in

*Corresponding author. Tel.: +1 217 244 7648; Fax: +1 217 244 0720
Email address: `geubelle@illinois.edu` (P. Geubelle)

these plies results in degraded material properties and often leads to further degradation of the laminate, such as induced delamination between plies and fiber breakage [2]. Characterizing and modeling the transverse failure of composites are complicated by the variability present not only in the material microstructure (i.e., the fiber size distribution and placement), but also in the local constitutive and failure properties of the constituents. The interaction between failure mechanisms such as fiber/matrix interface debonding and matrix cracking further complicates the prediction of the transverse strength of the composite laminate [1].

Multiple analytical and numerical models have been developed over the past decades to predict transverse cracking in composite laminates. In analytical models, it is often assumed that sequential cracks occur midway between existing cracks [3, 4], while numerical models, which tend to rely on periodic boundary conditions, simulate only a small portion of the experimental microstructure [5, 6, 7] and/or assume a uniform, structured packing [8, 9]. However, there is an increasing need to model larger, more realistic composite microstructures, as complex interactions between phases result in effective properties that are highly dependent on microstructural details [10].

In unidirectional composites with a high fiber volume fraction under transverse tensile loading, failure typically occurs at the interfaces between the fibers and the matrix. One of the most successful numerical methods used to capture this type of failure relies on a cohesive failure law relating the cohesive traction to the displacement jump along the fiber/matrix interfaces [11, 12]. This approach is also the basis of the present study, which relies on a nonlinear, discontinuous extension of a recently introduced Interface-enriched Generalized Finite Element Method (IGFEM) [13, 14] that allows for the modeling of transverse failure in realistic virtual composite microstructures with hundreds of fibers discretized with non-conforming finite element meshes. Beyond the development of this special form of the IGFEM, a key goal of this work is to compute the sensitivity of the transverse failure response of the transverse ply to the cohesive properties of the fiber/matrix interfaces. To that effect, we present an analytic material sensitivity formulation based on the direct differentiation method and implement it in the nonlinear, cohesive IGFEM solver. Related work on IGFEM-based sensitivity analysis in the context of multi-scale material design can be found in [15] and [16].

The manuscript is organized as follows: in Section 2, the material system of interest and experimental observations are presented. Next, Section 3 summarizes the computational method used to simulate the initiation and propagation of the transverse cracks. Section 4 describes the sensitivity analysis adopted in this work to capture the dependence of the transverse failure response of the transverse ply on the cohesive failure properties of the fiber/matrix interfaces. Additional derivations of the sensitivity to the critical displacement jumps are provided in the Appendix. The sensitivity formulations are verified against finite difference approximations in Section 5, while Section 6 summarizes the results of a sensitivity analysis performed on a virtual composite laminate composed of hundreds of fibers.

2. Experimental Observations

The material system under investigation is a $[0/90/0]_T$ composite laminate (Figure 1). The 90° ply is made of AS4 carbon fibers (Hexcel Corporation, Stamford, CT) embedded in an Araldite/Aradur 8605 epoxy system, while the 0° plies, which serve as barriers to the transverse cracks propagating in the 90° ply, consist of glass fibers (PPG industries, Pittsburgh, PA) in the same epoxy matrix. Glass fibers are used in the top and bottom layers to allow for the initiation of transverse cracks in the carbon/epoxy ply at lower loads. The manufacturing of the composite specimen involves using an in-house pre-impregnator to create pre-preg plies from a carbon fiber or glass fiber spool. The composites are consolidated under vacuum bag pressure and temperature according to manufacturer recommended cure cycle. The composite panels are then cut into rectangular coupons.

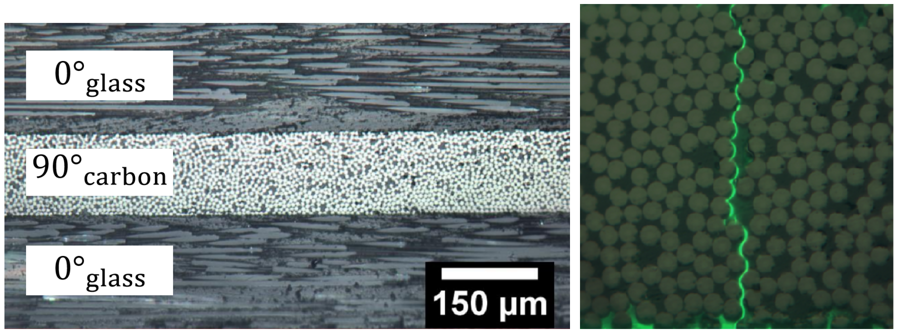

Figure 1: Left: Optical image of the $[0/90/0]_T$ composite laminate used in the transverse failure experiments. The 0° plies are glass/epoxy while the 90° ply consists of carbon fibers embedded in the epoxy matrix. Right: Representative image of a transverse crack spanning the 90° ply. The crack path was identified visually after unloading by the introduction of a fluorescent penetrant while the specimen is under loading. As apparent from this optical image, the transverse cracks extend primarily along fiber/matrix interfaces.

Six composite samples with thickness 0.7 mm, width 2 mm, and a guage length of 25 mm were tested in an Instron loadframe. The composite specimens were subjected to quasi-static longitudinal tension at a displacement rate of 5 $\mu m/sec$ (SEMtester, MTI Instruments, Albany, NY) to obtain the composite stress-strain response. A custom LabVIEW virtual instrument was used to record load and displacement data. Samples were loaded under an optical microscope (DMR-R, Leica Microsystems, Buffalo Grove, IL) to record failure mechanisms in the transverse ply optically during the test.

The main failure mechanisms in this composite system are fiber/matrix debonding and matrix cracking, and a typical transverse crack from these experiments is shown in Figure 1. A detailed analysis of the fracture surface indicates that transverse cracks predominantly (in excess of 95% of the crack path) extend along the fiber/matrix interfaces, in agreement with results reported in [17, 18]. This observation motivates the emphasis placed in this computational work on the cohesive modeling of the fiber/matrix interface failure, as described in Section 3.

Small windows of the 90° ply were imaged using a Leica DMR optical microscope with 50X objective to capture the microstructure with enough resolution (9.3

$pixels/\mu m$) to make morphological reconstruction possible. Otsu's method for thresholding [19] was used to reduce the image to a binary representation. This method computes an optimum threshold intensity level to separate the pixels in the image into two pixel classes following a bi-modal histogram to minimize intra-class variance. Computing a single global threshold value may not be appropriate in large images due to non-uniform contrast across the image, which makes it difficult to classify pixels as foreground or background based on pixel intensity [20]. For this reason, local threshold intensity values were used to threshold smaller portions of the microstructure.

The reconstruction of the microstructure used Generalized Hough transforms, which have been adopted by multiple previous studies to find geometric parameters describing instances of geometric shapes [21, 22]. We adopted the circular Hough transform to identify individual fibers in the experimental micrographs [23], as illustrated in Figure 2a. To avoid the stress singularity associated with direct fiber-fiber contact, a one-pixel minimum spacing between fibers is enforced, which is of the order of 100 nm (or about 1/70 of a typical fiber diameter) for the image presented.

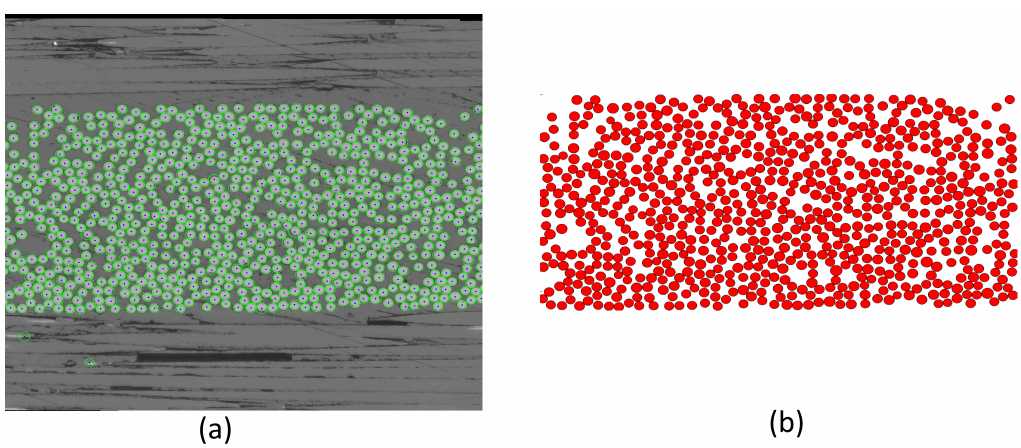

Figure 2: Reconstruction of fiber placement in the 90° ply.

The microstructure from Figure 2b, which is used in the simulations presented in Section 3, is composed of 751 fibers and has a fiber volume fraction of 55%. The fiber radius distribution is shown in Figure 3a, while the nearest-neighbor distance distribution is presented in Figure 3b, with the majority of fibers having a nearest neighbor closer than 135 nm.

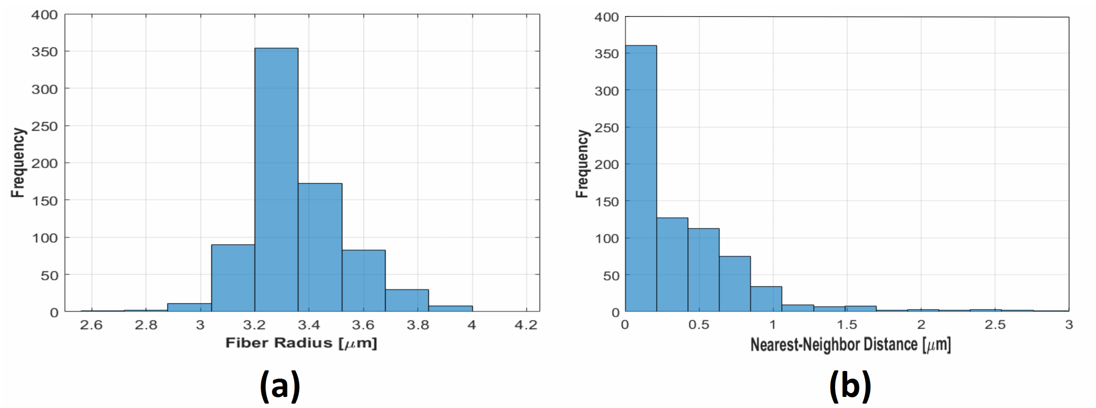

Figure 3: Fiber radius (a) and nearest-neighbor distance (b) distributions of the reconstructed composite microstructure taken from Figure 2b.

3. Modeling

To simulate the initiation and propagation of transverse cracks in the 90° ply, a plane strain finite element model is constructed directly from the reconstructed microstructure. As indicated earlier, the transverse cracks predominantly extend along the fiber/matrix interfaces, thereby motivating the use of a cohesive failure law to describe the progressive failure of the fiber/matrix interfaces.

One of the key challenges in modeling transverse failure in composite plies with high fiber volume fractions is associated with the very small distance between adjacent fibers. Using a conventional finite element method that relies on elements that conform to the fiber/matrix interfaces leads to extremely fine meshes, and therefore prohibitively expensive models. To address this challenge, which has limited most existing numerical analyses to small computational domains and/or unrealistically low fiber volume fractions, we have adopted a special form of a recently introduced IGFEM that allows for the modeling of non-conforming elements containing multiple cohesive interfaces.

Details on the numerical method adopted in this study are provided hereafter, together with the results of a typical mesoscale analysis of transverse failure in the $[0/90/0]_T$ laminate described in Section 2.

3.1. Cohesive Zone Model

For the cohesive failure of the fiber/matrix interfaces, we adopt the modified trilinear traction-separation law of Scheider *et al.* [24]. Five material properties characterize the cohesive response: the cohesive strength (σ_c), the three critical opening displacements (δ_{c1}, δ_{c2}, and δ_{c3}), and the ratio between shear and normal critical tractions (β). Defining the scalar effective displacement δ by

$$\delta = \sqrt{\beta^2\, \delta_s^2 + \delta_n^2}, \tag{1}$$

where δ_s and δ_n are the shear and normal components of the displacement jump vector ($\boldsymbol{\delta}$), the cohesive traction vector $\mathbf{t}$ takes the form

$$\mathbf{t} = \frac{t}{\delta}[\beta^2\, \boldsymbol{\delta} + (1-\beta^2)(\boldsymbol{\delta}\cdot\boldsymbol{n})\boldsymbol{n}], \tag{2}$$

where $\mathbf{n}$ is the normal vector of the interface and the scalar effective traction t is

$$t(\delta) = \sigma_c \begin{cases} 2(\frac{\delta}{\delta_{c1}}) - (\frac{\delta}{\delta_{c1}})^2 & \text{if } 0 \le \delta < \delta_{c1}, \\ 1 & \text{if } \delta_{c1} \le \delta < \delta_{c2}, \\ 2(\frac{\delta-\delta_{c2}}{\delta_{c3}-\delta_{c2}})^3 - 3(\frac{\delta-\delta_{c2}}{\delta_{c3}-\delta_{c2}})^2 + 1 & \text{if } \delta_{c2} \le \delta < \delta_{c3}, \\ 0 & \text{if } \delta \ge \delta_{c3}. \end{cases} \tag{3}$$

For unloading, when $\delta \le \delta_{max}$, a linear cohesive relation is adopted:

$$t = \frac{\delta}{\delta_{max}} t^*, \tag{4}$$

where $t^* = t(\delta_{max})$.

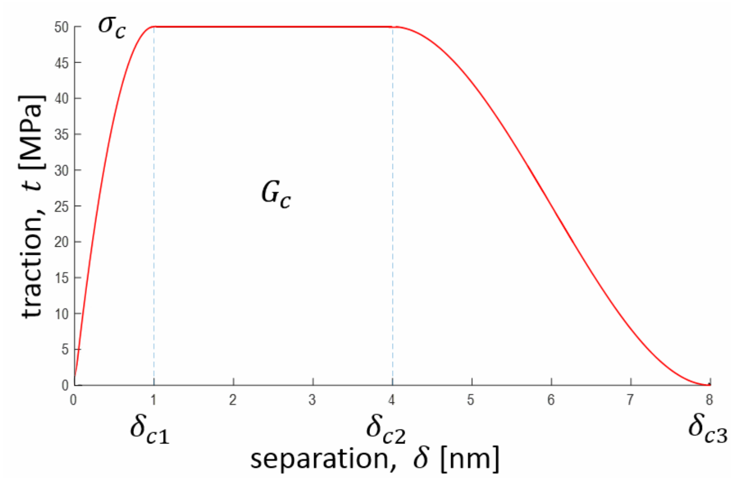

Figure 4: Smooth "trilinear" cohesive law corresponding to $\sigma_c = 50MPa$, $\delta_{c1} = 1nm$, $\delta_{c2} = 4nm$, and $\delta_{c3} = 8nm$. The area under the curve G_c denotes the cohesive fracture toughness of the fiber/matrix interface.

As shown in Figure 4, the nonlinear relations in the first and third segments of the cohesive law are introduced to ensure the C^1 continuity of the traction-separation law. The area under the traction-separation law, which denotes the cohesive fracture toughness, G_c, of the interface is given by

$$G_c = \sigma_c(\frac{\delta_{c2}}{2} + \frac{\delta_{c3}}{2} - \frac{\delta_{c1}}{3}). \tag{5}$$

The initial slope of the cohesive law, which describes the initial compliance of the cohesive interface prior to failure (i.e., for $\delta < \delta_{c1}$) is given by $2\sigma_c/\delta_{c1}$.

Finally, a numerical damping scheme is used to stabilize the solution [25]:

$$t = f(\sigma_c, \delta_{c1}, \delta_{c2}, \delta_{c3}, \beta) + \xi \frac{\sigma_c}{\delta_{c1}} \frac{d\delta}{dt}, \tag{6}$$

where the first term on the right-hand-side denotes the modified trilinear cohesive model described in Figure 4. To minimize the impact of the numerical damping term (ξ) on the solution, an adaptive scheme is adopted in which the damping parameter is progressively increased to the point where the solution is stabilized and decreased thereafter.

3.2. Interface-enriched Generalized Finite Element Method (IGFEM)

One of the key challenges in the modeling of transverse failure in composite layers with high fiber volume fraction is associated with the very small distance separating adjacent fibers. To address this challenge and allow for the simulation of transverse failure in realistic virtual models of a composite layer consisting of hundreds of closely packed fibers, we have adopted a special form of IGFEM. The method was originally introduced in [13, 14] to simulate the thermal and structural response of heterogeneous materials with meshes that do not conform to the material interfaces by using enrichment functions and generalized degrees of freedom that allow for capturing the gradient discontinuity present across these material interfaces.

For the present application, the method is modified in two ways. Firstly, while the traditional IGFEM utilizes C^0 enrichment functions to capture the gradient discontinuity of the solution across "intact" material interfaces, the method is extended hereafter to the use of C^{-1} enrichment functions to capture the discontinuity in the displacement solution field associated with the cohesive failure of the fiber/matrix interfaces [26]. In this discontinuous extension of the IGFEM, two enrichment nodes are placed at every intersection of the material interface with an element edge. Generalized degrees of freedom are then associated with the original enrichment node and its "mirror" node, allowing for the introduction of a cohesive failure model used to describe their progressive normal and tangential separations.

Beyond the ability to model cohesive failure with non-conforming discontinuous elements, the second modification to the conventional IGFEM used in this study consists of the introduction of enriched elements with two cohesive interfaces which are used to model the potential failure of two very close fiber/matrix interfaces when they intersect the same element [27].

The remainder of the implementation of the nonlinear IGFEM solver is relatively conventional and consists of a Newton-Raphson scheme with adaptive load stepping, and a parallel C++ framework using the Message Passing Interface (MPI). PETSc [28] is used to solve the linearized system of equations using Krylov subspace methods.

3.3. Mesoscale Simulations

The mesoscale computational model, created from the reconstructed microstructure shown previously in Figure 2b, is presented schematically in Figure 5, together with details of the non-conforming IGFEM mesh. The model, which spans the entire thickness of the 90° ply, contains 751 fibers. The width (L_1) is approximately 325 μm, the height of the 90° ply (H_2) is 162 μm and each of the 0° plies (H_1) has a height of 28 μm. The non-conforming triangular elements intersected by the fiber/matrix interfaces contain one or two cohesive interfaces. The other elements are conventional 3-node linear elements. The IGFEM computational model is made of $512,025$ elements, $321,975$ nodes, and $643,950$ degrees of freedom.

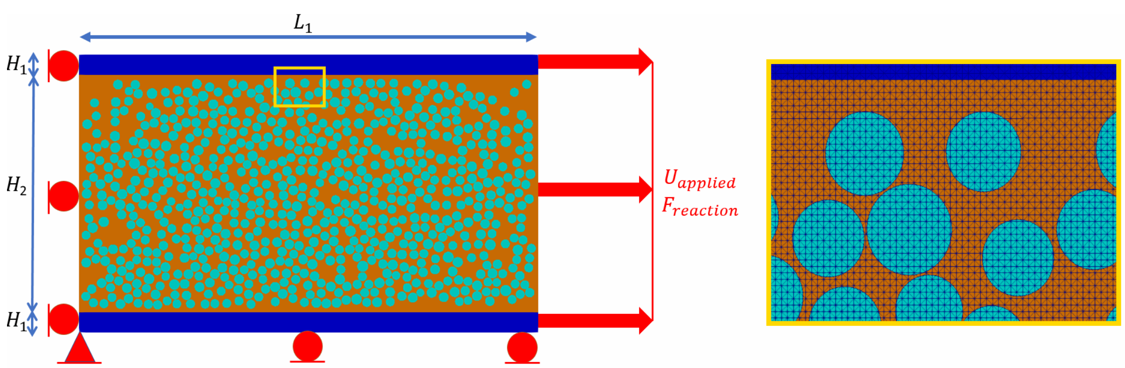

Figure 5: (Left) Schematic of mesoscale computational model used to simulate the transverse failure of the reconstructed microstructure shown in Figure 2b, with (right) details of the IGFEM mesh consisting of non-conforming triangular elements. Cohesive interfaces are placed along each fiber/matrix interface.

The in-plane properties of the various constituents are summarized in Table 1. The cohesive properties used to model the failure of the fiber/epoxy matrix interfaces are derived from a numerical analysis of microbond experiments [29]. The homogenized properties used in the 0° plies are obtained using the classical Halpin-Tsai relations [1, 30], with a fiber volume fraction of 69% in these 0° plies.

Table 1: Material properties used in the mesoscale simulations.

Carbon fibers	$E = 19.5\ GPa,$	$\nu = 0.45$	
Epoxy matrix	$E = 2.38\ GPa,$	$\nu = 0.43$	
Cohesive interfaces	$\sigma_c = 50\ MPa,$	$\delta_{c1} = 1\ nm,$	$\delta_{c2} = 4\ nm,$
	$\delta_{c3} = 8\ nm,$	$\beta = 1$	
0° glass-epoxy plies	$E_1 = 49.2\ GPa,$	$E_2 = 7.21\ GPa,$	$\nu_{12} = 0.298,$
	$G_{12} = 3.96\ GPa,$	$G_{23} = 2.08\ GPa$	

Under the effect of a 0.43% transverse strain, a complex heterogeneous stress state and transverse cracking pattern develop in the composite laminate, as illustrated in Figure 6a, in which the deformations have been scaled by a factor of five. The figure clearly shows distinct transverse cracks consisting of failed cohesive interfaces that span the 90° ply. Due to stiffness of the 0° plies, the corresponding evolution of the transverse stress (Figure 6b) computed from the reaction forces along the right edge of the computational domain remains almost linear up to the point where the cohesive elements in the vicinity of the crack path begin to fail and subsequently reduce the overall modulus of the composite.

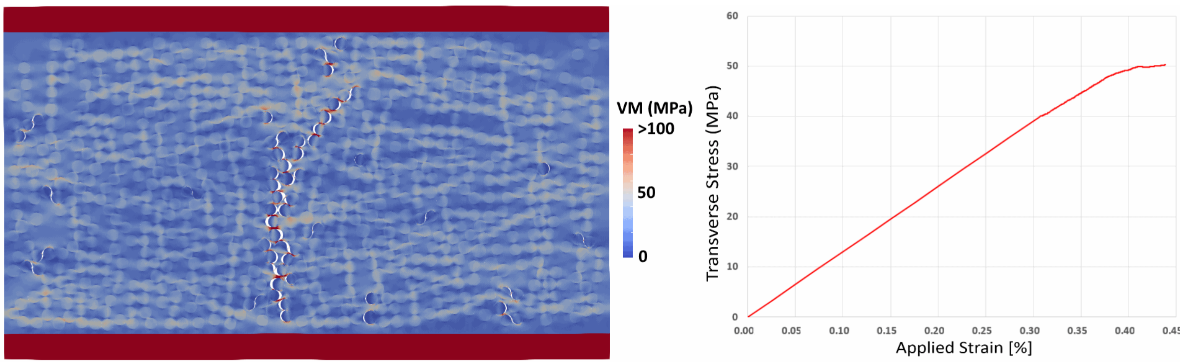

Figure 6: (Left) Von Mises stress distribution in the composite laminate subjected to a 0.43% applied transverse strain with the deformations scaled by a factor of five, showing the appearance of a transverse crack spanning the width of the 90° ply. (Right) Corresponding transverse stress-strain curve.

3.4. Validation

The IGFEM model for transverse composite failure was validated by comparing the statistical distribution of the predicted linear elastic response and onset of failure with experimental measurements. A reconstructed microstructure of approximately 6000 fibers was split into 9 and 18 sections of about 700 and 350 fibers, respectively. These results are compared with experimental measurements of the initial stiffness and of the strain at the first transverse crack obtained from tensile tests performed on the same $[0/90/0]_T$ carbon/glass-epoxy system, with the onset of transverse cracking captured through acoustic emission.

These virtual specimens were subjected to a tensile loading up to a transverse strain of about 0.5%. The resulting stress-strain curves are plotted in Figure 7 with the characteristic first crack marked for each computational case. The cohesive traction-separation law for this set of validation simulations is the same as outlined in Table 1 and the previous example of a mesoscale simulation using the IGFEM computational model. Table 2 presents a comparison between experimental and numerical values of the initial composite stiffness and the strain corresponding to the formation of the first transverse crack, measured through decreases in the macroscopic stress-strain curve, and indicates good agreement between measured and predicted values.

Table 2: Validation of computational model based on the initial composite stiffness and the strain at the onset of transverse cracking. N denotes the number of sections into which the large composite sample was split for the mesoscale validation. The experimental values of the initial stiffness are obtained by scaling the measured data using an isostrain relation of the $[0/90/0]_T$ laminate to reflect the reduced thickness of the simulated 0° plies.

	Initial stiffness [GPa]	Initial stiffness error [%]	Strain at first crack [%]	First crack error [%]
Experimental	14.03 ± 0.363	N/A	0.34 ± 0.06	N/A
IGFEM (N=9)	13.06 ± 0.396	6.91	0.345 ± 0.026	1.47
IGFEM (N=18)	12.80 ± 0.266	8.77	0.358 ± 0.022	5.29

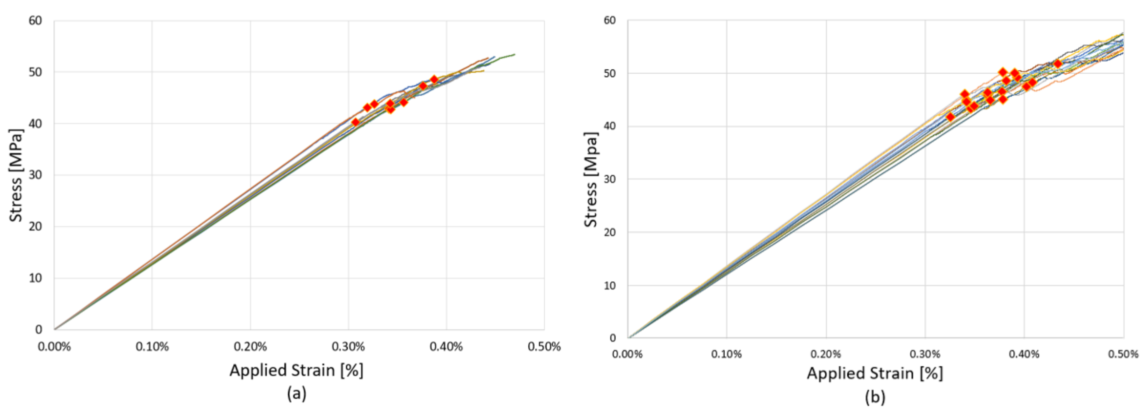

Figure 7: Numerical stress-strain curves associated with 9 (a) and 18 (b) virtual microstructures composed of approximately 700 and 350 fibers, respectively. The diamond-shaped symbols denote the strains at which the first transverse crack for each microstructure is predicted.

4. Sensitivity Analysis - Formulation

Beyond the simulation of transverse failure in realistic composite layers reconstructed directly from optical images, a key objective of this work is the analytical extraction of the sensitivity of the transverse failure response on the parameters defining the cohesive failure of the fiber/matrix interfaces. In particular, we derive the IGFEM-based analytic material sensitivity of the macroscopic transverse stress (denoted hereafter simply as σ) with respect to the interface variables (denoted as η_i). A direct method is used here because of the costly nature of the nonlinear simulations which would make finite difference extremely expensive, while the direct method allows us to compute sensitivities at very low cost.

For this problem, the response functional at every load step n can be written as

$$^{n}\sigma = \mathbf{L}^{T\,n}\mathbf{F}_p^{ext}\frac{1}{2H_1 + H_2}, \tag{7}$$

where $\mathbf{L}^T$ is a constant vector of 0's and 1's to select the correct degrees of freedom from the external force vector $\mathbf{F}^{ext}$, the subscript p denotes the prescribed degrees of freedom, and H_1 and H_2 are the ply thicknesses introduced in Figure 5. Unit depth is assumed here. The sensitivity of the macroscopic transverse stress at load step n with respect to the design variable η_i can then be expressed as

$$\frac{d^{n}\sigma}{d\eta_i} = \mathbf{L}^T\frac{d^{n}\mathbf{F}_p^{ext}}{d\eta_i}\frac{1}{2H_1 + H_2}. \tag{8}$$

The partitioned system of nonlinear equations,

$$^{n}\mathbf{F}^{int}\left(\eta_i, {}^{n-1}\boldsymbol{\delta}_{max}(\eta_i), {}^{n}\mathbf{U}(\eta_i, {}^{n-1}\boldsymbol{\delta}_{max}(\eta_i))\right) = \begin{bmatrix} ^{n}\mathbf{F}_f^{int} \\ ^{n}\mathbf{F}_p^{int} \end{bmatrix} = \begin{bmatrix} 0 \\ ^{n}\mathbf{F}_p^{ext} \end{bmatrix} = {}^{n}\mathbf{F}^{ext}, \tag{9}$$

where the subscript f denotes the free degrees of freedom, is solved incrementally. Because no external loads are applied, $^{n}\mathbf{F}_f^{ext}$ vanishes. $^{n}\boldsymbol{\delta}_{max}$ denotes the vector of internal state variables computed at each cohesive integration point:

$$^{n}\delta_{max} = \begin{cases} \sqrt{\beta^2\,{}^{n}\delta_s^2 + {}^{n}\delta_n^2} & \text{if loading,} \\ ^{n-1}\delta_{max} & \text{if unloading.} \end{cases} \tag{10}$$

Differentiation of (9) yields

$$ {}^{n}\mathbf{K}^{ff}\frac{d\,{}^{n}\mathbf{U}^{f}}{d\eta_i} = -\left(\frac{\partial\,{}^{n}\mathbf{F}_{f}^{int}}{\partial\eta_i} + \frac{\partial\,{}^{n}\mathbf{F}_{f}^{\;int}}{\partial\,{}^{n-1}\boldsymbol{\delta}_{max}}\frac{d\,{}^{n-1}\boldsymbol{\delta}_{max}}{d\eta_i}\right) \tag{11} $$

and

$$ \frac{d\,{}^{n}\mathbf{F}_{p}^{ext}}{d\eta_i} = {}^{n}\mathbf{K}^{pf}\frac{d\,{}^{n}\mathbf{U}^{f}}{d\eta_i} + \frac{\partial\,{}^{n}\mathbf{F}_{p}^{int}}{\partial\eta_i} + \frac{\partial\,{}^{n}\mathbf{F}_{p}^{\;int}}{\partial\,{}^{n-1}\boldsymbol{\delta}_{max}}\frac{d\,{}^{n-1}\boldsymbol{\delta}_{max}}{d\eta_i}. \tag{12} $$

Note that $\frac{d\,{}^{n}\mathbf{U}^{p}}{d\eta_i} = 0$ since ${}^{n}\mathbf{U}^{p}$ is a prescribed value applied at each load step. ${}^{n}\mathbf{K}^{ff}$ and ${}^{n}\mathbf{K}^{pf}$ are the partial derivatives of the free and prescribed internal force vectors with respect to the free displacements, respectively.

To compute $\frac{d\,{}^{n}\sigma}{d\eta_i}$ in Equation (8), the right-hand side of Equation (12) must be evaluated which requires the solution of the linear system given by Equation (11) to compute $\frac{d\,{}^{n}\mathbf{U}^{f}}{d\eta_i}$. The right-hand sides of Equations (11) and (12) contain the partial derivative of the internal force with respect to the internal variables ${}^{n-1}\boldsymbol{\delta}_{max}$, which is computed only over the cohesive elements. The elemental internal force vector contribution from a cohesive element has the form

$$ {}^{n}\mathbf{F}_{elem}^{int,\{cohesive\}} = \sum_{gp=1}^{n_{gp}} w_{gp}\mathbf{N}_{gp}^{T}\,{}^{n}\mathbf{t}_{gp}\,dA, \tag{13} $$

where w_{gp} is the Gauss integration weight, $\mathbf{N}_{gp}$ is a matrix arrangement of the discontinuous enrichment functions used to compute the displacement jump vector, and ${}^{n}\mathbf{t}_{gp}$ is the traction vector defined in Equation (2). Differentiating Equation (13) with respect to the internal variables yields

$$ \begin{aligned} \frac{\partial\mathbf{F}_{gp}^{int,\{cohesive\}}}{\partial\,{}^{n-1}\delta_{max}^{gp}} &= w_{gp}N_{gp}^{T}\frac{\partial\,{}^{n}\mathbf{t}_{gp}}{\partial\,{}^{n-1}\delta_{max}^{gp}}d\boldsymbol{A}, \\ \frac{\partial\,{}^{n}\mathbf{t}_{gp}}{\partial\,{}^{n-1}\delta_{max}^{gp}} &= \begin{cases} 0 & \text{if loading,} \\ \frac{1}{{}^{n-1}\delta_{max}^{gp}}\left(\frac{dt^*}{d\,{}^{n-1}\delta_{max}^{gp}} - \frac{t^*}{{}^{n-1}\delta_{max}^{gp}}\right)\left[\beta^2\,\boldsymbol{\delta} + (1-\beta^2)(\boldsymbol{\delta}\cdot\boldsymbol{n})\boldsymbol{n}\right] & \text{if unloading,} \end{cases} \end{aligned} \tag{14} $$

where t^* is defined in Equation (4) and $\frac{dt^*}{d\,{}^{n-1}\boldsymbol{\delta}_{max}}$ is easily computed from Equation (3).

The right-hand sides of Equations (11) and (12) also contain the derivatives of the internal variables with respect to the parameters from the previous load step. These derivatives are simply stored as additional internal variables for each quadrature point and initialized as $\frac{d^0\boldsymbol{\delta}_{max}}{d\eta_i} = 0$. For subsequent steps, the components of the vector are updated using

$$\frac{d^n\delta_{max}}{d\eta_i} = \begin{cases} \frac{1}{2\,{}^n\delta}(2\beta^2\,{}^n\delta_s \frac{d^n\delta_s}{d\eta_i} + 2\,{}^n\delta_n \frac{d^n\delta_n}{d\eta_i}) & \text{if loading,} \\ \frac{d^{n-1}\delta_{max}}{d\eta_i} & \text{if unloading,} \end{cases} \tag{15}$$

where

$$\frac{d^n\delta_{gp}}{d\eta_i} = \mathbf{N}_{gp}\frac{d^n\mathbf{U}_{elem}}{d\eta_i}. \tag{16}$$

In Equation (16), $\frac{d^n\mathbf{U}_{elem}}{d\eta_i}$ can be solved using Equation (11). These updated internal variable derivatives are then used used in the sensitivity analysis at the end of the next load step.

The last missing term is the partial derivative of the internal force with respect to specific interface parameters. The sensitivity derivations presented in the remainder of this section are specific to $\eta_i = \sigma_c$, leaving a summary of the derivations of the sensitivity with respect to the critical displacement jumps δ_{ci} $(i = 1, 2, 3)$ for the Appendix.

Again, the contributions from the linear elastic bulk elements to the partial derivative vanish as the stress does not depend explicitly on the cohesive internal strength. The partial derivative of Equation (13) with respect to σ_c is

$$\frac{\partial^n\mathbf{F}^{int,\{cohesive\}}_{elem}}{\partial\sigma_c} = \sum_{gp=1}^{n_{gp}} w_{gp}\mathbf{N}^T_{gp}\frac{\partial^n\mathbf{t}_{gp}}{\partial\sigma_c}dA. \tag{17}$$

The explicit partial derivative of Equation (2) with respect to σ_c yields

$$\frac{\partial^n\mathbf{t}_{gp}}{\partial\sigma_c} = \frac{\partial^n t}{\partial\sigma_c}\frac{1}{{}^n\delta}[\beta^2\,{}^n\boldsymbol{\delta} + (1-\beta^2)({}^n\boldsymbol{\delta}\cdot\boldsymbol{n})\boldsymbol{n}], \tag{18}$$

where $\frac{\partial t}{\partial \sigma_c}$ is readily obtained from Equation (3) as

$$\frac{\partial t}{\partial \sigma_c} = \begin{cases} 2(\frac{\delta}{\delta_{c1}}) - (\frac{\delta}{\delta_{c1}})^2 & \text{if } 0 \leq \delta < \delta_{c1}, \\ 1 & \text{if } \delta_{c1} \leq \delta < \delta_{c2}, \\ 2(\frac{\delta-\delta_{c2}}{\delta_{c3}-\delta_{c2}})^3 - 3(\frac{\delta-\delta_{c2}}{\delta_{c3}-\delta_{c2}})^2 + 1 & \text{if } \delta_{c2} \leq \delta < \delta_{c3}, \\ 0 & \text{if } \delta \geq \delta_{c3}. \end{cases} \tag{19}$$

5. Sensitivity Analysis - Verification

To verify the material sensitivity analysis described in Section 4, the simple problem shown in Figure 8 is solved. The verification problem consists of a small square domain containing two fibers of different sizes. The larger and smaller fibers have a diameter of 8 μm and 6 μm, respectively, which correspond to the upper and lower sizes of the carbon fibers used in the experiments.

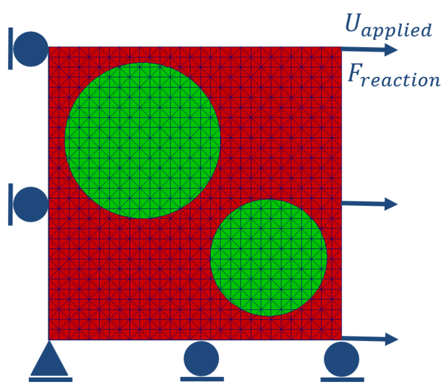

Figure 8: Schematic of two-fiber problem used to verify the analytic sensitivity formulation.

The cohesive properties for this simulation are chosen as $\sigma_c = 50\ MPa$, $\delta_{c1} = 10\ nm$, $\delta_{c2} = 40\ nm$, $\delta_{c3} = 80\ nm$, and $\beta = 1$. The domain is subjected to a 2% traverse strain and the results computed by the direct analytical sensitivity formulation described in the previous section are compared to those obtained with a central finite difference scheme.

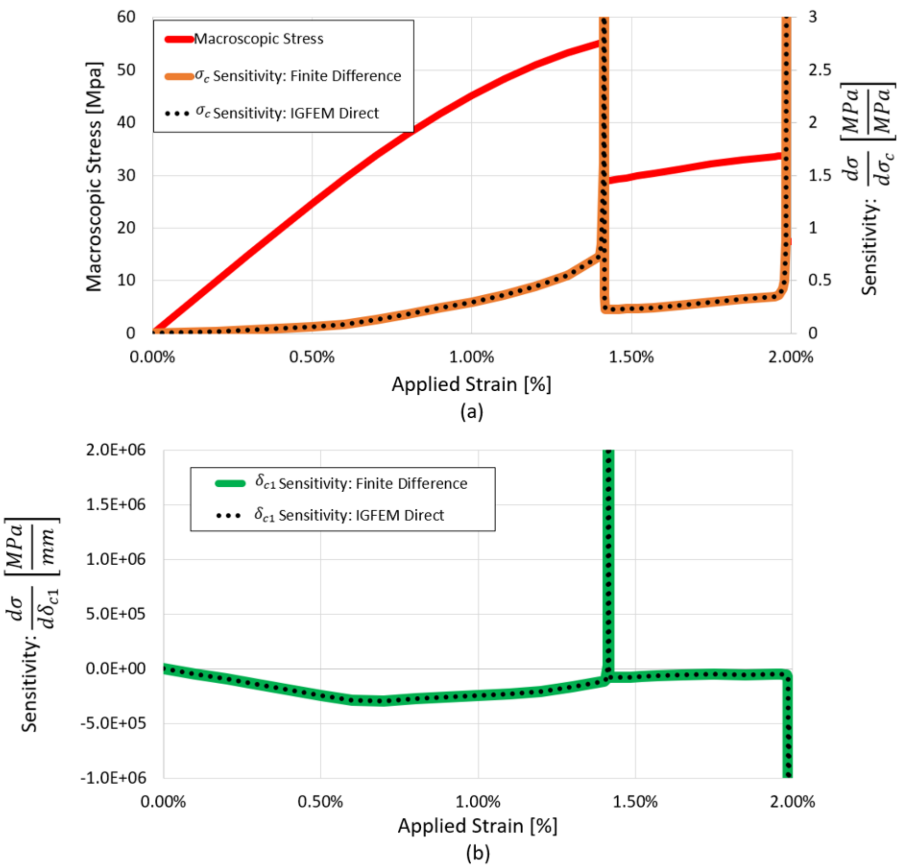

Figure 9: Verification of the material sensitivities for the two-fiber problem shown in Figure 8. (a) Transverse stress-strain response and sensitivity of the transverse stress with respect to σ_c; (b) Sensitivity with respect to δ_{c1}.

As shown in Figure 9, there is a very good agreement between the analytic and finite difference sensitivity results for both the sensitivities with respect to the cohesive strength and to δ_{c1}. The first and second peaks observed in the sensitivity curves are associated with the debonding failure of the larger and smaller fibers, respectively. As expected, the sensitivity of the transverse stress with respect to σ_c remains positive through the entire range of applied strains as the incremental increase of the cohesive strength leads to an overall increase of σ over the entire traction-separation curve as seen in Figure 10 which shows the effect of differential changes in both σ_c and δ_{c1} on a example traction-separation curve. The sensitivity of the transverse stress with respect to δ_{c1} is first negative, as a higher value of the critical displacement jump for a fixed cohesive strength leads to a more compliant cohesive model, and therefore a decrease in σ. Once the interfaces start to fail, the δ_{c1} sensitivity of σ switches sign, as a larger value of δ_{c1} leads to a delayed failure, and therefore a higher value of σ for a given applied strain.

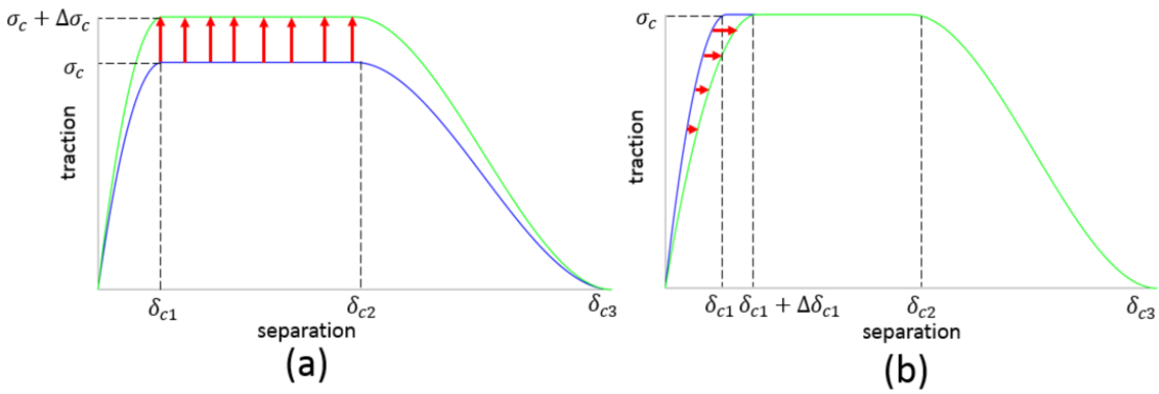

Figure 10: Schematic illustration of the impact on the cohesive traction-separation curve for an incremental increase in σ_c (a) and in δ_{c1} (b).

6. Sensitivity Analysis - Results

In this section, a 406-fiber microstructure is simulated to extract the sensitivity of the transverse stress with respect to the cohesive strength and the critical displacement jumps. The simulated microstructure is presented in Figure 11 at $\epsilon_{\text{applied}} = 0.5\%$ showing a large transverse crack. The macroscopic transverse stress curve, along with the evolution of the sensitivity with respect to the cohesive strength, is plotted against the applied strain in Figure 12, and the sensitivities with respect to the critical displacement jumps are presented in Figure 13.

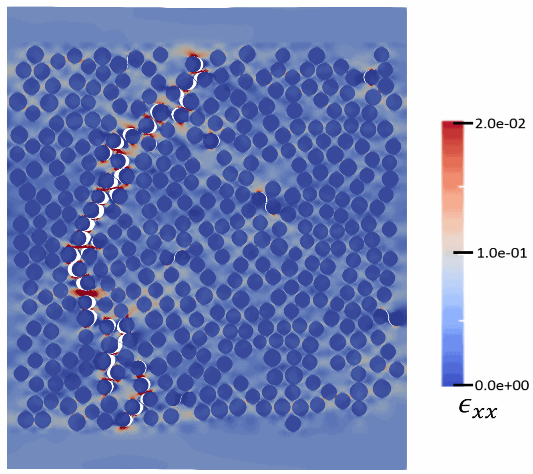

Figure 11: Formation of a large transverse crack at 0.5% strain in the 90° ply of the $[0/90/0]_T$ composite laminate. The 90° ply is composed of 406 fibers. The deformation has been scaled by a factor of five.

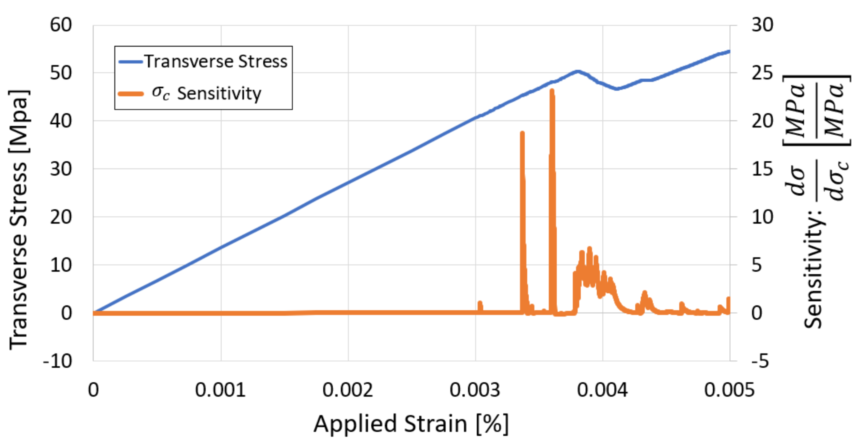

Figure 12: Evolution of the transverse stress σ and of the σ_c-sensitivity of σ versus the applied transverse strain for the 406-fiber problem shown in Figure 11.

As apparent in Figure 12, the sensitivity of the transverse stress-strain curve with respect to σ_c remains positive throughout the transverse failure process. This result can be again explained by the effect of differential changes in σ_c on the cohesive law illustrated in Figure 10a.

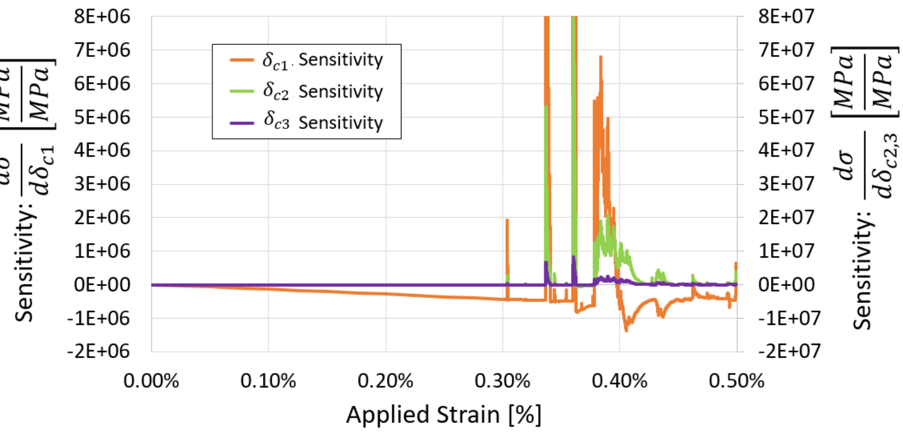

Figure 13: Evolution of the sensitivities of the transverse stress σ with respect to the critical displacement jumps δ_{ci} for the trilinear cohesive law versus the applied transverse strain for the 406-fiber problem.

The sensitivity of the transverse stress with respect to δ_{c1} is initially negative due to the increase cohesive compliance of the interfaces, as illustrated in Figure 10b. During the failure events the δ_{c1}-sensitivity becomes positive due to the delayed failure response. The sensitivities with respect to δ_{c2} and δ_{c3} initially vanish before becoming positive during the failure events. It should also be noted that the sensitivity with respect to δ_{c3} is substantially smaller than the sensitivity with respect to δ_{c2}.

Due to the complexity of the large 406-fiber microstructure and of the stress field in the 90° ply, the failure of the fiber/matrix interfaces is a complex function of the applied strain, rendering a precise determination of the onset of transverse cracking difficult when only inspecting the stress-strain response or deformed geometry. However, the evolution of the sensitivities of the transverse stress with respect to the cohesive parameters provides a clear insight on the correlation between applied strain and the onset of transverse cracking.

7. Conclusion

A computational framework has been presented for the modeling of transverse cracking in realistic virtual microstructures of 90° composite plies reconstructed directly from optical images. The underlying numerical method relies on a discontinuous, multi-interface extension of an Interface-enriched Generalized Finite Element Method, which allows for the simulation of fiber/matrix debonding in composite layers with high fiber volume fractions. This computational model has been validated against strain measurements of the onset of transverse cracking performed on a $[0/90/0]_T$ carbon/glass-epoxy laminate. Also included in the computational framework is the analytic extraction of the sensitivity of the macroscopic transverse stress with respect to the parameters that define the cohesive failure law. By monitoring the evolution of these sensitivities, the onset and propagation of transverse cracks can be assessed. It should be noted, however, that in the present study all fiber/matrix interfaces are assumed to have the same cohesive properties. The next steps include relaxing that assumption and deriving individual interface property sensitivities, i.e., extracting how sensitive the transverse stress is to the critical stress of individual fibers. With these individual sensitivities, one could study the sensitivity to the parameters that define the distributions of the interface properties, e.g., the sensitivity to the average and standard deviation of the interface strength.

Acknowledgements

This work has been supported through a grant No. FA9550-12-1-0445 to the Center of Excellence on Integrated Materials Modeling (CEIMM) at Johns Hopkins University (partners JHU, UIUC, UCSB), awarded by the AFOSR/RSL (Computational Mathematics Program, Manager Dr. A. Sayir) and AFRL/RX (Monitors Dr. C. Woodward and C. Przybyla).

References

[1] I. Daniel, O. Ishai, Engineering Mechanics of Composite Materials, Oxford University Press, 2005.

[2] J. Nairn, Matrix microcracking in composites, in: Comprehensive Composite Materials, Elsevier, 2000, Ch. 2, pp. 403–432.

[3] K. Garrett, J. Bailey, Multiple transverse fracture in 90° cross-ply laminates of a glass fibre-reinforced polyester, Journal of Materials Science 12 (1977) 157–168.

[4] J. Mayugo, P. Camanho, P. Maimi, C. Davila, Analytical modelling of transverse matrix cracking of $[\pm\theta/90_n]_s$ composite laminates under multiaxial loading, Mechanics of Advanced Materials and Structures 17 (2010) 237–245.

[5] L. Canal, J. Segurado, J. LLorca, Failure surface of epoxy-modified fiber-reinforced composites under transverse tension and out-of-plane shear, International Journal of Solids and Structures 46 (2009) 2265–2274.

[6] D. O'Dwyer, N. O'Dowd, C. McCarthy, Numerical micromechanical investigation of interfacial strength parameters in a carbon fibre composite material, Journal of Composite Materials 48 (6) (2014) 749–760.

[7] A. Louhghalam, S. Arwade, Prediction of incipient damage sites in composites using classifiers, International Journal of Damage Mechanics 19 (2010) 233–260.

[8] T. Okabe, M. Nishikawa, H. Toyoshima, A periodic unit-cell simulation of fiber arrangement dependence on the transverse tensile failure in unidirectional carbon fiber reinforced composites, International Journal of Solids and Structures 48 (2011) 2948–2959.

[9] T. Okabe, H. Sekine, K. Ishii, M. Nishikawa, N. Takeda, Numerical method for failure simulation of unidirectional fiber-reinforced composites with spring element model, Composites Science and Technology 65 (2005) 921–933.

[10] S. Torquato, Random Heterogeneous Materials, Microstructure and Macroscopic Properties, Springer, 2002.

[11] T. Vaughan, C. McCarthy, Micromechanical modelling of the transverse damage behaviour in fibre reinforced composites, Composites Science and Technology 71 (2011) 388–396.

[12] V. Kushch, S. Shmegera, P. Brondsted, L. Mishnaevsky, Numerical simulation of progressive debonding in fiber reinforced composite under transverse loading, International Journal of Engineering Science 49 (2011) 17–29.

[13] S. Soghrati, A. Aragón, C. Duarte, P. Geubelle, An interface-enriched generalized finite element method for problems with discontinuous gradient fields, International Journal of Numerical Methods in Engineering 89 (8) (2012) 991–1008.

[14] S. Soghrati, P. Geubelle, A 3D interface-enriched generalized finite element method for weakly discontinuous problems with complex internal geometries, Computer Methods in Applied Mechanics and Engineering 217-220 (2012) 46–57.

[15] A. Najafi, M. Safdari, D. Tortorelli, P. Geubelle, A gradient-based shape optimization scheme using an interface-enriched generalized FEM, Computer Methods in Applied Mechanics and Engineering 296 (2015) 1–17.

[16] A. Najafi, M. Safdari, D. Tortorelli, P. Geubelle, Material design using a NURBS-based shape optimization scheme, in: In 57th AIAA/ASCE/AHS/ASC Structures, Structural Dynamics, and Materials Conference, American Institute of Aeronautics and Astronautics Inc, AIAA., 2016.

[17] T. Hobbiebrunken, M. Hojo, T. Adachi, C. D. Jong, B. Fiedler, Evaluation of interfacial strength in CF/epoxies using FEM and in-situ experiments, Composites Part A: Applied Science and Manufacturing 37 (2006) 2248–2256.

[18] E. Gamstedt, B. Sjogren, Micromechanisms in tension-compression fatigue of composite laminates containing transverse plies, Composites Science and Technology 59 (1999) 167–178.

[19] N. Otsu, A threshold selection method from gray-level histograms, IEEE Transaction on Systems, Man, and Cybernetics 9 (1979) 62–66.

[20] M. Chandrakala, P. Devi, Threshold based segmentation using block processing, International Journal of Innovative Research in Computer and Communication Engineering 4 (2016) 821–826.

[21] D. Ballard, Generalizing the Hough transform to detect arbitrary shapes, Pattern Recognition 13 (1981) 111–122.

[22] T. Atherton, D. Kerbyson, Size invariant circle detection, Image and Vision Computing 17 (1999) 795–803.

[23] C. Przybyla, T. Godar, S. Bricker, J. Simmons, M. Jackson, L. Zawada, J. Pearce, Statistical characterization of SiC/SiC ceramic matrix composites at the filament scale with bayesian segmentation, Hough transform feature extraction, and pair correlation statistics, in: International SAMPE Technical Conference, 2013, pp. 859–878.

[24] I. Scheider, W. Brocks, The effect of the traction separation law on the results of cohesive zone crack propagation analyses 251 (2003) 313–318.

[25] Y. F. Gao, A. F. Bower, A simple technique for avoiding convergence problems in finite element simulations of crack nucleation and growth on cohesive interfaces, Modelling and Simulation in Materials Science and Engineering 12 (3) (2004) 453.

[26] A. Aragón, A. Simone, The discontinuity-enriched finite element method, International Journal for Numerical Methods in Engineering 112 (2017) 1589–1613.

[27] S. Zacek, Exploring the link between microstructure statistics and transverse ply fracture in carbon/epoxy composites, Master's thesis, University of Illinois - Urbana-Champaign (2017).

[28] S. Balay, S. Abhyankar, M. F. Adams, J. Brown, P. Brune, K. Buschelman, L. Dalcin, V. Eijkhout, W. D. Gropp, D. Kaushik, M. G. Knepley, L. C. McInnes, K. Rupp, B. F. Smith, S. Zampini, H. Zhang, H. Zhang, PETSc Web page, http://www.mcs.anl.gov/petsc (2016).

[29] S. Potukuchi, Fracture analysis of carbon fiber/epoxy matrix interface through microbond and cruciform tests, Master's thesis, University of Illinois - Urbana-Champaign (2016).

[30] J. Halpin, J. Kardos, The Halpin-Tsai equations: A review, Polymer Engineering and Science 16 (1976) 344–352.

Appendix A. Sensitivity to Critical Displacement Jumps

For completeness, a summary of the sensitivity formulation with respect to the critical displacement jumps δ_{c1}, δ_{c2}, and δ_{c3} is included hereafter, starting from Equation (18) in Section 4.

For linearly elastic volumetric elements, again there is no explicit dependence of the internal force contribution on δ_{ci} and no displacement discontinuity. Therefore, Equation (18) simply becomes

$$\frac{\partial^n \mathbf{t}_{gp}}{\partial \delta_{ci}} = \frac{\partial^n t}{\partial \delta_{ci}} \frac{1}{^n\delta}[\beta^2\, {}^n\boldsymbol{\delta} + (1-\beta^2)({}^n\boldsymbol{\delta}\cdot\boldsymbol{n})\boldsymbol{n}]. \tag{A.1}$$

From Equation (3), the partial derivatives of the scalar effective traction are

$$\frac{\partial t}{\partial \eta_i} = \begin{cases} \begin{cases} -2\sigma_c \left(1 - \frac{\delta_e}{\delta_{c1}}\right)\left(\frac{\delta_e}{\delta_{c1}^2}\right) & 0 \le \delta_e < \delta_{c1} \\ 0 & \text{else} \end{cases} & \text{for } \eta_i = \delta_{c1} \\ \begin{cases} 6\sigma_c \left(\frac{\delta_e - \delta_{c2}}{\delta_{c3} - \delta_{c2}} - 1\right)\left(\frac{\delta_e - \delta_{c2}}{\delta_{c3} - \delta_{c2}}\right)\left(\frac{\delta_e - \delta_{c3}}{(\delta_{c3} - \delta_{c2})^2}\right) & \delta_{c2} \le \delta_e < \delta_{c3} \\ 0 & \text{else} \end{cases} & \text{for } \eta_i = \delta_{c2} \\ \begin{cases} -6\sigma_c \left(\frac{\delta_e - \delta_{c2}}{\delta_{c3} - \delta_{c2}} - 1\right)\left(\frac{\delta_e - \delta_{c2}}{\delta_{c3} - \delta_{c2}}\right)\left(\frac{\delta_e - \delta_{c2}}{(\delta_{c3} - \delta_{c2})^2}\right) & \delta_{c2} \le \delta_e < \delta_{c3} \\ 0 & \text{else.} \end{cases} & \text{for } \eta_i = \delta_{c3} \end{cases} \tag{A.2}$$